

# Integrated Massively Parallel Simulation of Thermo-Electromagnetic Fields and Transients of Converter Transformer Interacting With MMC in Multi-Terminal DC Grid

Peng Liu , *Student Member, IEEE*, Ning Lin , *Student Member, IEEE*,  
and Venkata Dinavahi , *Senior Member, IEEE*

**Abstract**—A computationally efficient model to study the transient interaction of the finite-element (FE) converter transformer with modular multi-level converter (MMC) can provide the advanced knowledge of the field-circuit interactions that can be utilized for the design and test of equipment; however, the runtime of existing simulation tools developed for CPU execution usually takes days or even weeks, which is prohibitively long. In this paper, an integrated thermo-electromagnetic model is proposed for the transient simulation of FE-based transformer interacting with the MMC in a multi-terminal dc grid, with the magnetic field, thermal field, and electrical networks fully coupled. The transmission-line modeling solution is employed for the nonlinear FE problem, and each MMC is split into a number of minimum possible circuits, so that the codes can be sufficiently parallelized and implemented on the graphics processing unit with thousands of Cuda cores to be runtime friendly. The integrated model can provide the transient field distributions within the transformer and the device-level information of the MMC such as switching transients and junction temperatures. Compared with a commercial software package, the execution time of  $10^5$  time-steps decreased from several days to only hours with a speedup of more than 47 times while maintaining high accuracy.

**Index Terms**—Computational electromagnetics, electromagnetic transients (EMTs), field-circuit coupling, finite-element (FE) method, high-voltage direct current, modular multi-level converter (MMC), multi-domain, multi-physics, parallel processing, power transformer, transmission-line matrix (TLM) method.

## I. INTRODUCTION

**M**ULTI-PHYSICS simulation software combining finite element analysis (FEA) and electromagnetic transient (EMT) program has gained increasing significance for the design, prototyping, evaluation, and validation of components in high power applications [1]. The device-level modeling enables more accurate and comprehensive information that is

Manuscript received February 7, 2019; revised April 13, 2019; accepted May 4, 2019. Date of publication May 29, 2019; date of current version June 11, 2020. This work was supported by the Natural Science and Engineering Research Council of Canada. (*Corresponding author: Ning Lin.*)

The authors are with the Department of Electrical and Computer Engineering, University of Alberta, Edmonton, AB T6G 1H9 Canada (e-mail: pliu3@ualberta.ca; ning3@ualberta.ca; dinavahi@ualberta.ca).

Color versions of one or more of the figures in this paper are available online at <http://ieeexplore.ieee.org>.

Digital Object Identifier 10.1109/TEMC.2019.2915340

unavailable in system-level study, such as the magnetic field distribution revealed by a finite-element (FE) power transformer model for saturation analysis and eddy-current distribution for total loss calculation, the exact performance of a power electronic switching unit, and the impacts including rise in junction temperature [2]–[4]. However, the notorious computational burden of the FE solver and the efficiency of the EMT program are usually the main bottleneck, especially in large-scale ac/dc grids with multiple transformers where the field-circuit coupling is involved [5]–[8].

Simulation tools for the analysis of EMT in power systems and power electronic circuits can be classified into two categories: 1) system-level (such as PSCAD/EMTDC, Simulink, EMTP-RV) and 2) device level (such as SaberRD, PSpice, and Ansys Simplorer). On the other hand, field-oriented tools such as FLUX CEDRAT, Comsol ac/dc and Ansys Maxwell usually focus on the physical details such as geometries and material properties of electromagnetic devices. For a system-level simulation including FE models, a field-circuit coupling technique is normally required. Although FLUX CEDRAT and Comsol ac/dc provide the field-circuit interface, the built-in electrical components in their libraries are very limited and only include basic  $R$ ,  $L$ , and  $C$  elements. The co-simulation between Ansys Simplorer and Ansys Maxwell is capable of large-scale power electronic circuit simulation including FE components [8]–[10]; however, the execution time will be prohibitively long to run a large number of time-steps.

Modern high-performance massively parallel architectures such as graphics processing units (GPUs) and CPU clusters have been utilized to improve the efficiency of field computation [11]–[15] and power electronics [16], [17], and the key of performance improvement, according to the Amdahl's law [18], is determined by the parallelism of the program. Considering the computational load balance and potential to be parallelized, the well-known transmission-line matrix (TLM) modeling, which solves the nonlinearity at the elemental level, has been employed in the solution phase of nonlinear FE problems [19], [20], to exploit parallelism and improve the computational efficiency.

So far, no research work has been reported to study the interaction of the modular multi-level converter (MMC) and FE

transformer model, not to mention high-performance massively parallelized codes running on GPU. Under this background, an integrated thermo-electromagnetic model combining the FE transformer model and the MMC is established to study their transient interaction in this paper. The FE method is utilized to calculate both the Ampere's law for magnetics and the Fourier's law for heat conduction, and the interfaces between the magnetic field, thermal field, and electrical networks are fully considered. The integrated model can provide detailed field distributions within the transformer and device-level information of the MMC under transient conditions. The codes are massively parallelized for execution on NVIDIA Tesla V100 GPU [21], and the run-time is over 47 times faster than that of the Ansys Simplorer and Ansys Maxwell co-simulation.

The contributions of this paper are listed as follows.

- 1) The transmission-line modeling, which solves the nonlinearities at the elemental level and thus is decentralized in nature, is employed to solve the nonlinear FE equations in a massively parallel manner.
- 2) The electrical network, thermal field, and magnetic field are fully coupled by exchanging coupling coefficients. The thermal impact of winding loss and eddy-current loss are considered for the computation of magnetic field and electrical network.
- 3) Fully detailed modeling of the MMC whose EMT topology is reconfigured using circuit partitioning, which separates all the submodules (SMs) from their arms to create a substantial number of independent sub-circuits that cater to parallel processing.
- 4) The interaction of FE transformer model and MMC is implemented with an indirect field-circuit coupling scheme, and the FE transformer is represented by nonlinear self- and mutual-inductances whose values can be extracted from the FE-element computation.
- 5) The massive parallelism of the integrated codes is sufficiently explored to execute on massive parallel GPU architectures.

The paper is organized as follows: Section II describes the integrated thermo-electromagnetic transformer model and the coupling techniques in details, and Section III provides the electro-thermal model of the IGBT in the MMC. Section IV illustrates the parallel implementation of the integrated model on GPU. Then, Section V gives the case studies and result comparisons, and at last, Section VI presents the conclusion.

## II. COUPLED THERMO-ELECTROMAGNETIC MODEL OF CONVERTER TRANSFORMER

### A. FE Model for Magnetic Field

Consider the two-dimensional (2-D) FE model in Fig. 1 for a power transformer rated 230 kV/110 kV and 400 MVA. For low- and medium-frequency applications, the magnetic field generated by the winding currents is governed by the Ampere's law

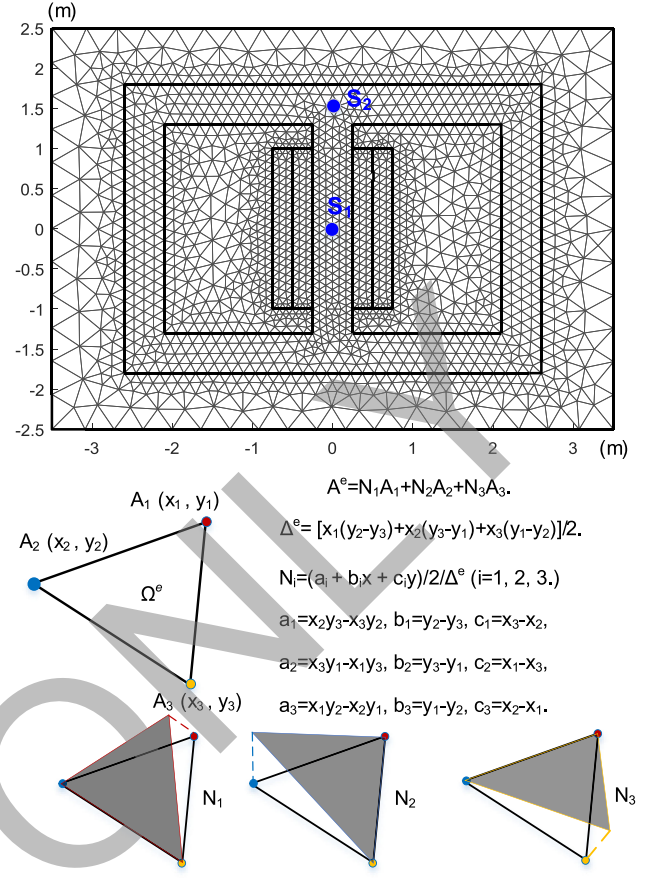


Fig. 1. 2-D transformer model using the Galerkin FE method.

with unknown magnetic vector potential. We have the following:

$$\nabla \cdot (v \nabla A) = \sigma \frac{\partial A}{\partial t} - J \quad (1)$$

where  $v$  is the field-dependent reluctivity,  $\sigma$  the electrical conductivity, and  $J$  the impressed current density.

After applying the Galerkin FE method, the elemental equation for each triangular element can be obtained [20] as

$$\begin{aligned} \frac{v^e}{4\Delta^e} \begin{bmatrix} k_{11} & k_{12} & k_{13} \\ k_{21} & k_{22} & k_{23} \\ k_{31} & k_{32} & k_{33} \end{bmatrix} \begin{bmatrix} A_1 \\ A_2 \\ A_3 \end{bmatrix} + \frac{\sigma^e \Delta^e}{12} \begin{bmatrix} 2 & 1 & 1 \\ 1 & 2 & 1 \\ 1 & 1 & 2 \end{bmatrix} \begin{bmatrix} \frac{\partial A_1}{\partial t} \\ \frac{\partial A_2}{\partial t} \\ \frac{\partial A_3}{\partial t} \end{bmatrix} \\ = \frac{J_z^e \Delta^e}{3} \begin{bmatrix} 1 \\ 1 \\ 1 \end{bmatrix}. \end{aligned} \quad (2)$$

The nonlinear  $B-H$  curve of the transformer core can be found in [22], and the magnetic vector potentials on the artificial boundaries are assumed to be 0.

The elemental equations can be assembled to a global nonlinear system to solve, or alternatively, the equation is equivalent to the nonlinear electrical network in Fig. 2(b) and can be solved using the TLM scheme wherein the component values are given

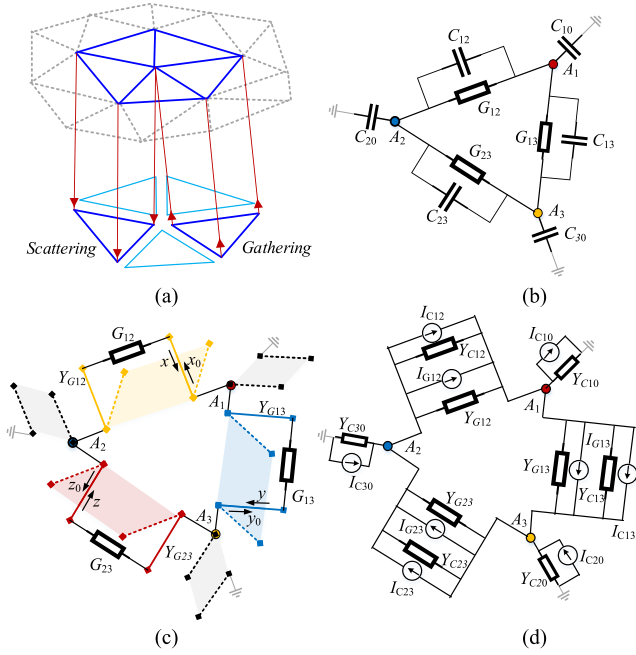


Fig. 2. TLM solution for the nonlinear 2-D FE problem. (a) 2-D Triangular mesh. (b) Equivalent nonlinear network. (c) TLM model: Scattering. (d) TLM model: Gathering.

as follows:

$$\begin{aligned}
 G_{12} &= -\frac{v^e}{4\Delta^e}(b_1b_2 + c_1c_2), & Y_{G12} &= -\frac{v_g^e}{4\Delta^e}(b_1b_2 + c_1c_2) \\
 G_{13} &= -\frac{v^e}{4\Delta^e}(b_1b_3 + c_1c_3), & Y_{G13} &= -\frac{v_g^e}{4\Delta^e}(b_1b_3 + c_1c_3) \\
 G_{23} &= -\frac{v^e}{4\Delta^e}(b_2b_3 + c_2c_3), & Y_{G23} &= -\frac{v_g^e}{4\Delta^e}(b_2b_3 + c_2c_3) \\
 C_{12} = C_{13} = C_{23} &= -\frac{\sigma^e \Delta^e}{12}, & Y_{C12} = Y_{C13} = Y_{C23} &= -\frac{\sigma^e \Delta^e}{6\Delta t} \\
 C_{10} = C_{20} = C_{30} &= \frac{4\sigma^e \Delta^e}{12}, & Y_{C10} = Y_{C20} = Y_{C30} &= \frac{4\sigma^e \Delta^e}{6\Delta t}.
 \end{aligned} \tag{3}$$

The TLM scheme has perfect parallelism in the scattering phase and constant admittance matrix in the gathering phase. In the scattering phase [see Fig. 2(c)], the incident pulses based on the nodal solution are injected into each triangular element, and the reflected pulses can be calculated individually within each element; thus, the nonlinearity is treated in a massively parallel manner. In the gathering phase [see Fig. 2(d)], the reflected pulses enter the linear network as new incident pulses, and in order to obtain the new reflected pulses, a linear network is required to be solved, whose admittance matrix is determined by the characteristic impedance of the imagined transmission lines and generally remains unchanged. Thus, repeated updation and factorization of the Jacobian matrix in traditional nonlinear FE solver is circumvented, and the TLM technique is felicitous for parallel-computing architectures.

Note that the source term in (1) is the impressed current density determined by the winding currents. If the electrical networks are connected to the primary or secondary windings

(see Fig. 1), the winding currents are not known; thus, a field-circuit coupling scheme is required. In addition, the electrical conductivities of both the winding and transformer core are usually altered by the Joule effects of the winding loss and the eddy-current loss; thus, a thermal model is required.

### B. FE Model for Heat Conduction

The Fourier's law governing the heat transfer can be expressed by the following partial differential equation:

$$\nabla \cdot (\lambda \nabla T) = \rho C \frac{\partial T}{\partial t} - q \tag{4}$$

where  $\lambda$  is the thermal conductivity,  $\rho$  is the volumetric mass,  $C$  is the heat capacity, and  $q$  the heat source.

The elemental equation has similar form to that of (2), and the natural convective boundary conditions are employed. We have

$$\lambda \frac{\partial T}{\partial n} = h(T - T_0) \tag{5}$$

where  $n$  denotes the outward normal direction on the boundary,  $h$  the convection coefficient, and  $T_0$  the external environmental temperature.

Although the thermal conductivity,  $\lambda$ , depends on the temperature, implying that (4) is also nonlinear. Since the temperature field changes much slower than the EMTs, thus for simplification, the historical value of  $\lambda$  from the previous time-step is utilized so that the thermal problem becomes linear.

The heat sources originate from the Joule loss in the winding and eddy-current loss in the transformer core, and the changing temperature also alters the electrical conductivities of the transformer. In this paper, the winding material is copper and the transformer core is made of electrical steel, and their conductivities,  $\sigma(T)$ , altered by the temperature can be represented [23] as

$$\frac{1}{\sigma(T)} = \frac{1}{\sigma_0} + \alpha(T - T_0) \tag{6}$$

where  $T_0$  is the ambient temperature, and the parameters are provided in the Appendix.

### C. Multi-Domain Interfacing

Since the integrated model consists of three domains: the 1) external electrical network; 2) magnetic field; and 3) thermal field, there exist three kinds of interfaces between them, which are illustrated in Fig. 3(a).

The interfaces of the thermal field with the other two domains are quite direct: The external electrical network can provide the time-varying winding currents; thus, the Joule-type loss in the copper windings is available. The time-varying magnetic field will induce electrical field in the steel transformer core, and the eddy-current losses can also be obtained after post-processing. Naturally, both the winding loss and eddy-current loss are fed to the thermal field as heat sources. In turn, the thermal field updates the temperature distribution at each time-step, and the conductivities of the copper winding and steel transformer core are altered because of the change in temperature.

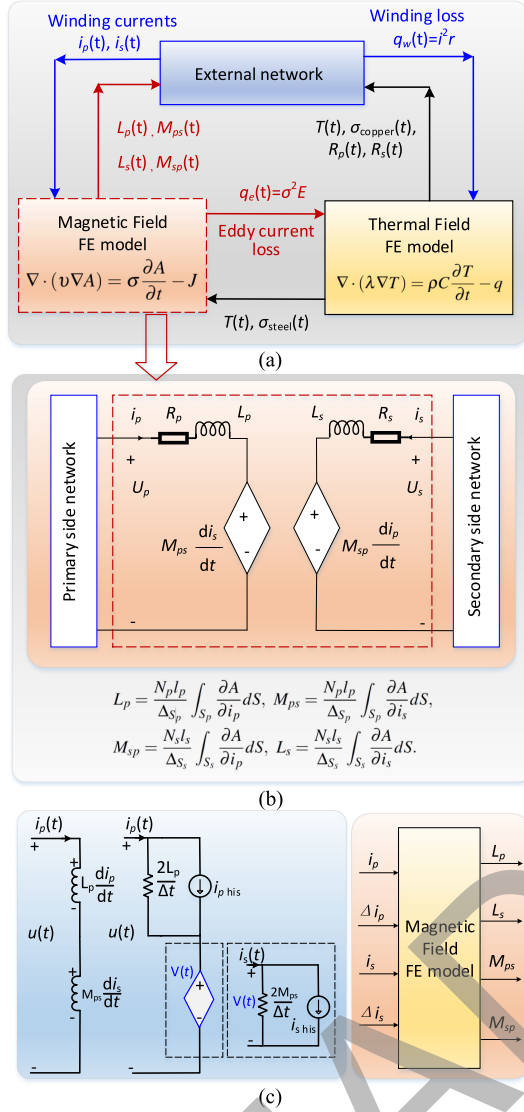


Fig. 3. (a) Interface of the external electrical network, magnetic field, and thermal field. (b) FE transformer represented by self- and mutual-inductances in electrical networks. (c) Trapezoidal rule applied for the discretization of self- and mutual-inductances.

For the interface between the external network and magnetic field, the coupling coefficients are the self- and mutual-inductances. According to the Faraday's law, the induced winding voltage can be calculated as

$$U = rI + \frac{Nl}{\Delta_S} \int_S \frac{\partial A}{\partial t} dS \quad (7)$$

where  $I$  is the winding current,  $r$  the winding resistance,  $N$  the number of turns,  $l$  the axial length of each filament,  $S$  the winding zone, and  $\Delta_S$  the area of the winding zone.

Equation (7) can be rewritten as the following on the basis of the partial differential chain rule:

$$U = rI + \frac{Nl}{\Delta_S} \int_S \frac{\partial A}{\partial i_p} dS \frac{\partial i_p}{\partial t} + \frac{Nl}{\Delta_S} \int_S \frac{\partial A}{\partial i_s} dS \frac{\partial i_s}{\partial t}. \quad (8)$$

Applying (8) to the primary and secondary windings, respectively, the self- and mutual-inductances of the transformer can

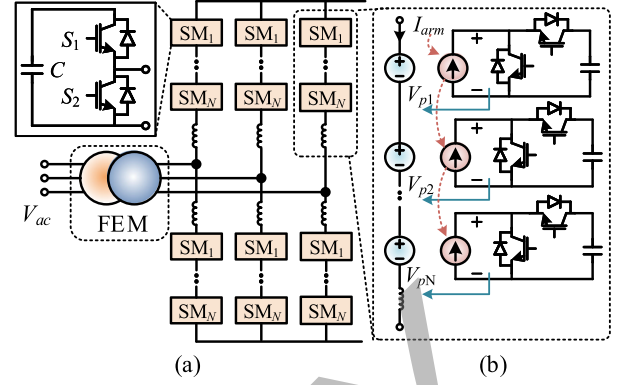


Fig. 4. Three-phase MMC-based HVdc converter station: (a) half-bridge MMC in connection with FEM-based converter transformer, and (b) MMC SM partitioning.

be extracted as

$$\begin{aligned} L_p &= \frac{N_p l_p}{\Delta_{S_p}} \int_{S_p} \frac{\partial A}{\partial i_p} dS, \quad M_{ps} = \frac{N_p l_p}{\Delta_{S_p}} \int_{S_p} \frac{\partial A}{\partial i_s} dS \\ M_{sp} &= \frac{N_s l_s}{\Delta_{S_s}} \int_{S_s} \frac{\partial A}{\partial i_p} dS, \quad L_s = \frac{N_s l_s}{\Delta_{S_s}} \int_{S_s} \frac{\partial A}{\partial i_s} dS. \end{aligned} \quad (9)$$

Fig. 3(b) shows how the FE transformer model is represented by an equivalent network composed of winding resistance, self-, and mutual-inductances, in order to be coupled with the external network, and these nonlinear inductance values are updated by the FE computation for different winding currents at each time-step.

In the EMT simulation, an inductance  $L$  can be represented by an impedance of  $2L/\Delta t$  in parallel with a historical current term using the Trapezoidal rule. Similarly, as shown in Fig. 3(c), the mutual inductance is equivalent to a current-differential controlled voltage source whose value is determined by the mutual inductance and the corresponding branch current after applying the Trapezoidal rule. For example, the KVL equation for the branch in Fig. 3(c) can be written as

$$u(t) = \frac{2L_p}{\Delta t} (i_p(t) - i_{p,his}) + \frac{2M_{ps}}{\Delta t} (i_s(t) - i_{s,his}). \quad (10)$$

Thus, the mutual inductances serve as active sources, and the magnetic field and electrical network are fully coupled. In addition, (10) implies that the primary-side network and the secondary-side network are fully coupled by the mutual inductances and, therefore, should be solved simultaneously as one system.

### III. ELECTRO-THERMAL MODELING OF THE MMC

In addition to the thermo-electromagnetic FE transformer model described above, the main contributor of the nonlinearity to the MMC shown in Fig. 4(a) is the power semiconductor switch IGBT and its anti-parallel diode. As the layout corresponds to a large admittance matrix due to the cascaded SMs, they are separated by circuit partitioning by using a pair of coupled voltage and current sources [24], and the reconfigured

MMC EMT arm model is given in Fig. 4(b). The arm current  $I_{\text{arm}}$  is sent to each MMC SM, and in return, the SM terminal voltage  $V_p$  is fed back to the arm. It can also be seen that after splitting each SM, the remaining circuit of the MMC is linear.

The prevalent ideal switch model [25] taken as a two-state resistor falls short of revealing a higher-than-normal current stress and the power dissipation during the IGBT switching period. Therefore, the dynamic curve-fitting model, which reproduces the shapes of transient waveforms, is selected for the comprehensive electro-thermal simulation. The rise and fall times denoted by  $t_r$  and  $t_f$ , respectively, are two key parameters reflecting the switching period. Their sensitivity to operation conditions such as collector current, gate resistance, and the junction temperature is tested and provided in the datasheet by the manufacturer. Therefore, they can be uniformly expressed by the following polynomial function:

$$t_{r,f}(x_1, x_2, x_3) = A_0 \cdot \prod_{i=1}^3 x_i + \sum_{\substack{k \neq j \\ k,j=1,2,3}} A_k x_k x_j + \sum_{m=1}^3 C_m x_m + C_0 \quad (11)$$

where  $A$  and  $C$  are coefficients, and  $x$  represents the factors affecting the switching time of the IGBT.

The actual switching waveforms can be divided into multiple sections depending on the curvatures, and then approximated by first-order circuits. For example, the experimental current waveform of the selected IGBT module 5SNA 2000K450300 [26] in Fig. 5(a) shows that the initial part of the turn-ON process can be taken as a straight line. Afterward, the rising rate decreases, and eventually the current falls till entering the steady state. Therefore, the turn-ON current can be simulated by an  $RL$  circuit excited by a per-unit voltage source,  $V_e$ , and the inductor current is regulated by changing the resistor, as shown in Fig. 5(b). The linear current at stage  $S_1$  is simulated by charging a pure inductor, followed by a varying slope, which is approximated by the  $RL$  circuit with an exponential function. The descending waveform starting at  $t_2$  is realized by removing the voltage source,  $V_e$ , so that the inductor discharges exponentially. Therefore, the inductor current in the per-unit circuit can be summarized as

$$i_L = \begin{cases} \frac{V_e}{L}(t_1 - 0), & 0 \leq t \leq t_1 \\ \frac{V_e}{R}(1 - e^{-\frac{t-t_1}{\tau}}), & t_1 \leq t \leq t_2 \\ \frac{I_0}{I_0} + i_L^{\max} e^{-\frac{t-t_2}{\tau}}, & t_2 \leq t \leq t_3 \end{cases} \quad (12)$$

where  $I_0$  is the steady-state current and  $i_L^{\max}$  the inductor's maximum current in per unit. Then, the inductor current is amplified by  $K$  times to simulate the actual device current. Similarly, the device turn-OFF transients can also be modeled by the first-order circuits.

As a critical part to compose an integral device-level switch model, the transient electro-thermal impedance is based on the

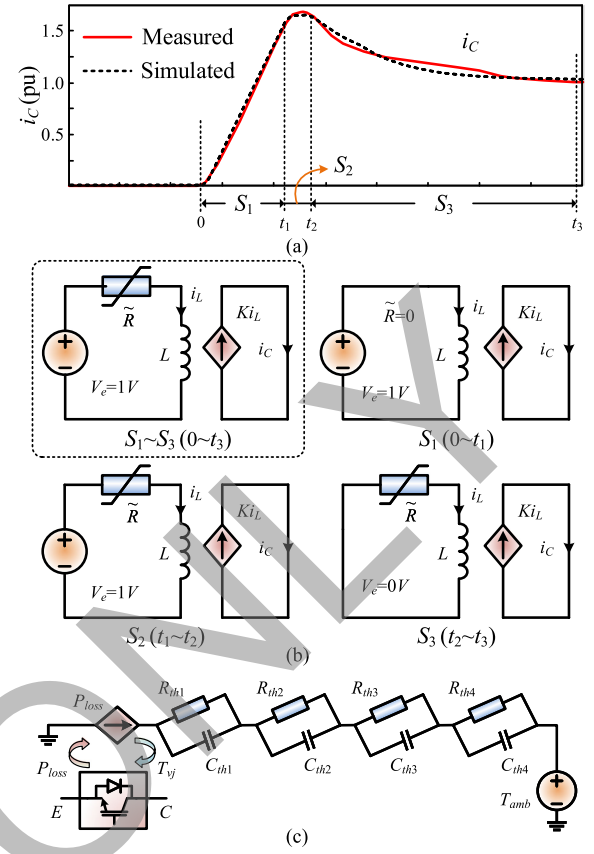


Fig. 5. IGBT electro-thermal curve-fitting model: (a) turn-ON current, (b) realization by first-order circuit, and (c) EMT model of the transient thermal impedance.

following analytical function:

$$Z_{\text{th}} = \sum_{i=1}^n R_{\text{th}(i)} (1 - e^{-\frac{t}{\tau_i}}) \quad (13)$$

where the impedance,  $R_{\text{th}(i)}$ , along with the time constant,  $\tau_i$ , can be realized by a paralleled  $RC$  pair for the EMT simulation, as given in Fig. 5(c) where

$$C_{\text{th}(i)} = \frac{\tau_i}{R_{\text{th}(i)}}. \quad (14)$$

In the equivalent circuit of the transient thermal impedance, the input-controlled current source is numerically equal to the power loss, and its terminal voltage is deemed as the semiconductor's junction temperature,  $T_{vj}$ . With the inherent cooling mechanism, the IGBT is exposed to the environment, and, therefore, the other terminal of the  $RC$  pairs is connected to a constant voltage source denoting the ambient temperature,  $T_{\text{amb}}$ , which is 25 °C.

#### IV. PARALLEL IMPLEMENTATION OF INTEGRATED FIELD-CIRCUIT MODEL ON THE GPU

The detailed program flow, data path, coupling coefficients, and block connections are illustrated in Fig. 6. The FE transmission-line modeling (FE-TLM) solution of the nonlinear magnetic field is provided in details, and the parallelism of each

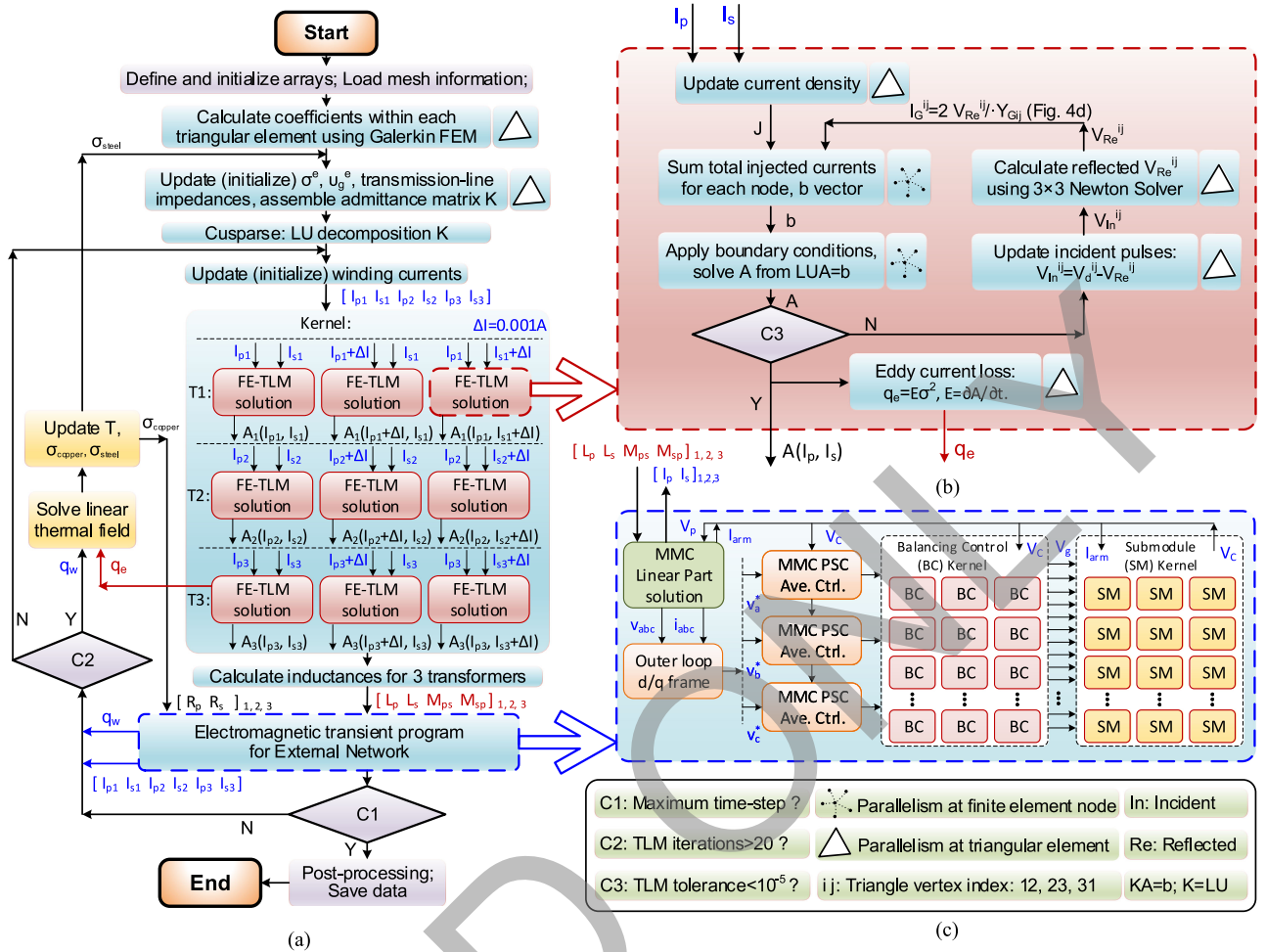


Fig. 6. Detailed massively parallel implementation of the integrated thermo-electromagnetic model on the GPU. (a) Program flowchart. (b) Finite element-transmission line modeling solution. (c) External network solution.

functional block, either at the nodal or the elemental level, is also noted. These blocks are all optimized to fit the Kernel functions in Cuda codes.

The program starts with loading the mesh information such as nodal coordinates and node–element connections; thus, the coefficients of Galerkin’s finite element method (FEM) in (2) and (3) can be obtained. According to Fig. 2(d) and (3), the admittance matrix of the linear network in the gathering phase is determined by two factors: 1) the guessed reluctivities  $v_g^e$  and 2) conductivities  $\sigma^e$  in each triangular element. Because of the thermal effects, the  $\sigma^e$  of the transformer core may be altered by the temperature, implying that the admittance matrix should be reassembled and decomposed occasionally. Meanwhile, the adaptive transmission-line impedances, using the solved  $v^e$  of the previous time-step instead of guessed  $v_g^e$ , can also be incorporated into the admittance matrix to efficiently reduce the required number of TLM iterations. In fact, the thermal field has a much larger time constant compared with that of the electromagnetic field, meaning that the temperature  $T(t)$  and  $\sigma^e(T)$  change much slower than electromagnetic parameters, so the admittance matrix does not have to be updated at each time-step. To balance the required number of TLM iterations and the computational costs of matrix decomposition, the criteria to update

the admittance matrix is determined by whether the required number of TLM iterations is more than 20, which is described as C2 (Condition 2) in Fig. 6.

Since the thermal field is assumed a linear FE problem, its description is simplified in the flowchart.

The field–circuit coupling scheme described before is applicable to every single-phase transformer independently, and each consists of three FE blocks to calculate the partial differentials in (9). Fig. 6 shows three single-phase transformers in an MMC-based HVdc station with nine FE blocks executed in parallel on the GPU. Once the magnetic vector potentials are calculated, the self- and mutual-inductances in (9) can be obtained for each transformer.

The details of each FE-TLM block are also provided, which includes TLM iterations: the scattering phase with elemental parallelism and the gathering phase with nodal parallelism. The summation of total currents into each node can be executed in parallel with appropriate information of node–element connections, and the LU solution process, which essentially is mere backward and forward substitutions, can also be parallelized. Once the network is updated, the nodal differences are available, and the incident pulses for the next TLM iteration can be obtained by subtracting the reflected pulse from the nodal

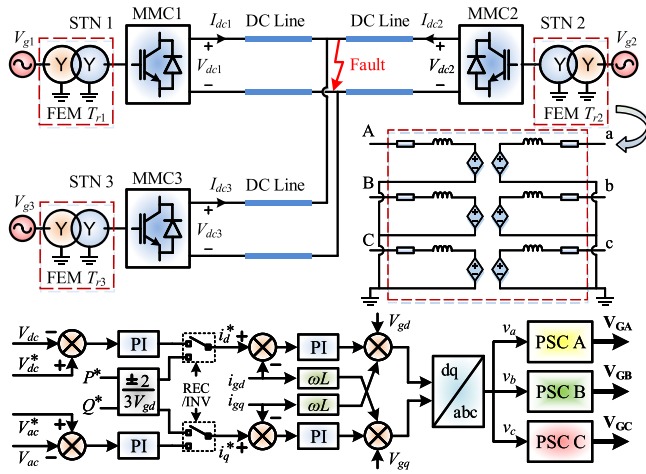


Fig. 7. Three-terminal HVdc system involving FEM transformer model.

difference. With the updated incident pulses, in order to obtain the reflected pulses from the triangular edges decoupled by the transmission line, a  $3 \times 3$  nonlinear system associated with the  $B-H$  curve needs to be solved, which requires several (generally 5–15) iterations of updating and solving the  $3 \times 3$  Jacobian matrix using the Cramer's rule [19], [20].

In the circuit domain, the MMC model is then computed following the update of the transformers' inductances. The linear subsystem as part of the field-circuit interface is connected directly to the transformers, while other parts, including the controller, are interactive internally. The solution of the interface gives the transformers' primary and secondary currents, which are returned to stage C2. Inside the MMC, the outer-loop controller regulates either power or dc voltage after transforming the grid voltage and current into the  $d-q$  frame, and the inner-loop controller adopting phase-shift control (PSC) strategy contains two parts: 1) the averaging control and 2) balancing control (BC) [27]. The converter modeling conforms to parallelism to expedite the simulation by functionally decomposing the MMC including its controller into multiple parts, which correspond to various kernels shown in Fig. 6(c). For example, the averaging control kernel  $Ave$  has three threads for each HVdc station; however, the output of the BC is gate signal  $V_g$ , which drives a switch in the SM directly, and, therefore, the BC kernel invokes an identical number of threads to the SM kernel, and both of them are a major contributor to the speedup because of their large quantity. The only signals that the MMC's linear part receives from other MMC blocks are the SM terminal voltages,  $V_p$ , in order to complete the computation.

## V. CASE STUDY AND RESULTS

### A. Case Description and Setup

Fig. 7 shows the 3-terminal dc system where the MMC-based stations,  $STN1$  and  $STN3$ , are rectifier stations, while the inverter station is denoted as  $STN2$ . All the converter transformers,  $T_{r1-3}$ , adopt the proposed FE model, and the geometric parameters of the FE transformer in Fig. 1 are presented in the Appendix. Each three-phase transformer is built from three single-phase transformers, as shown in Fig. 6; therefore, there

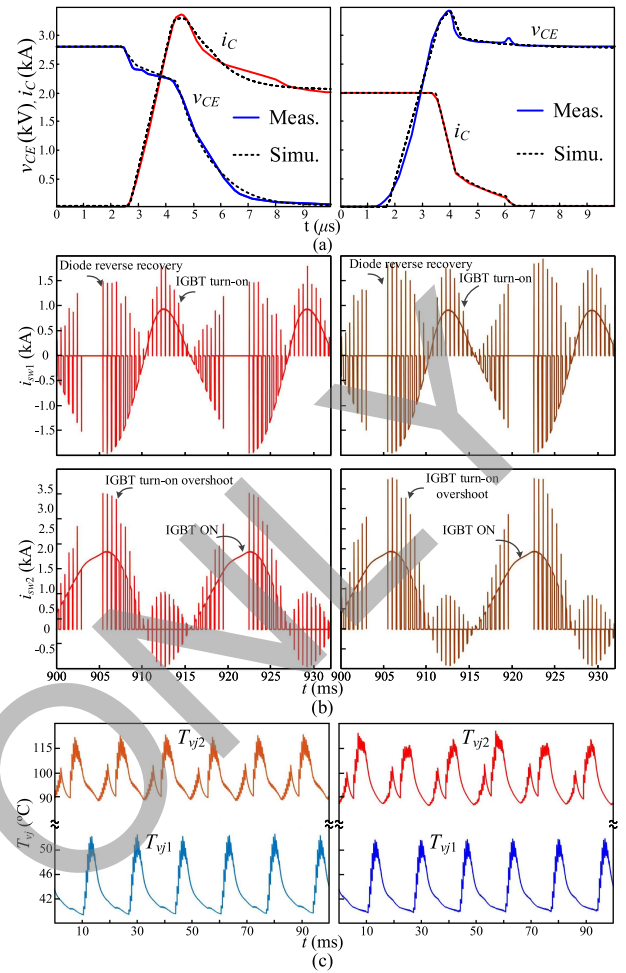


Fig. 8. IGBT device-level waveforms: (a) switching transients (proposed model: concrete line; experiment: dashed line), (b) upper switch current, (c) lower switch current, and (d) junction temperatures [(b)–(d) left: proposed model; right: SaberRD].

are nine independent single-phase transformers in total, and the inductance calculations can be executed in parallel. The HVdc converter control is conducted in the  $d-q$  frame, and depending on the role, the rectifier station regulates the active power in the  $d$ -axis, while the inverter station controls the terminal dc voltage,  $V_{dc2}$ . Since these converter stations are connected by the dc transmission lines, the dc voltages at the two rectifier stations,  $V_{dc1}$  and  $V_{dc3}$ , are slightly higher than those of their counterpart. After applying the inverse Park transformation, the three-phase signals,  $v_{a,b,c}$ , are sent to individual MMC inner-loop controller, which adopts the PSC strategy where the gate signals for the IGBTs are eventually generated.

### B. External Network Simulation Results

The device-level performance of the IGBT is given in Fig. 8, where SaberRD simulation results are also provided for validation. Fig. 8(a) gives the experimental IGBT turn-ON and turn-OFF waveforms and the simulated results of the proposed dynamic curve-fitting method. It shows that the linear and non-linear curves at various stages can be approximated by using the proposed multi-section functions as in (12). Fig. 8(b)–(c) is

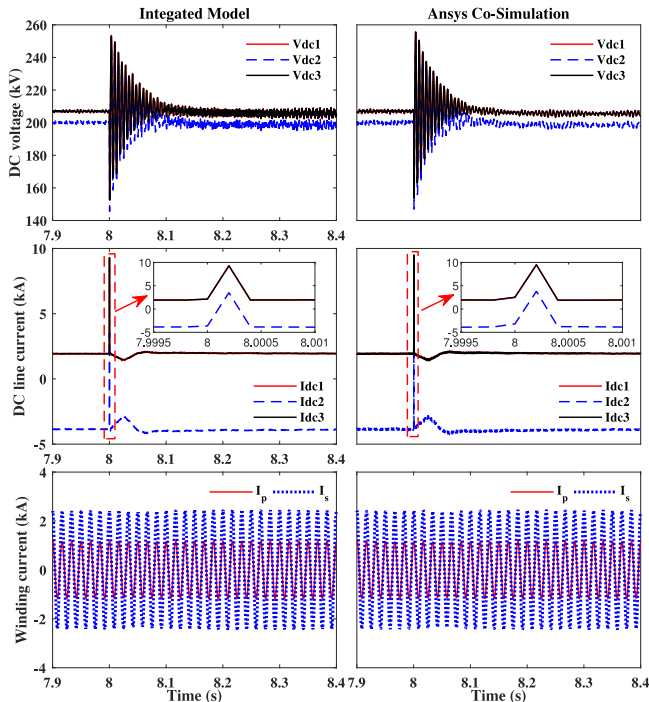


Fig. 9. MTdc system performance under short-term dc line-line fault.

obtained from a single-phase 5-level MMC with a dc-link voltage of 16 kV. The scale of the system is smaller than that of an HVdc station because of the limited capability of SaberRD in solving IGBT nonlinearities; nevertheless, it is sufficient for validating the device-level performance of the proposed IGBT model. The turn-ON current overshoot and diode reverse recovery current can be observed in the upper and lower switches in an MMC SM, and the results from the proposed model demonstrate a great similarity to those of the off-line simulation tool, including the junction temperatures.

Fig. 9 shows the system-level performance of the multi-terminal dc (MTdc) system subjected to short-term dc line-line fault. Initially, the dc voltage at the inverter station is exactly 200 kV, and the two rectifier stations have a slight margin as a result of power transfer, as it can be seen that the dc currents are around 2 kA at these two stations and 4 kA at the inverter station. At  $t = 8$  s, the fault lasting 200  $\mu$ s occurs in the middle of the line, and consequently, the profound impacts can be observed in the dc network. The dc voltages witness severe oscillations before being restored by the inverter 100 ms later; while the currents first see a dramatic rise and then restore after the fault disappears—the inverter current even witnesses a polarity reversal. On the other hand, the impact on the ac side is negligible since the currents on both the sides of the transformer remain maintained throughout the entire process. The above statements are validated by the right column sub-figure, where identical waveforms from Ansys co-simulation are given.

The power reversal as a typical system-level operation is also conducted in Fig. 10. Starting at  $t = 8$  s, the power reference at Station 1 is ordered to rise from 200 to 500 MW in a time gap of 2 s, while Station 3 as the other rectifier maintains its power order. It is observed that during the process, the dc voltages are largely stable, with only slight perturbations. As a consequence,

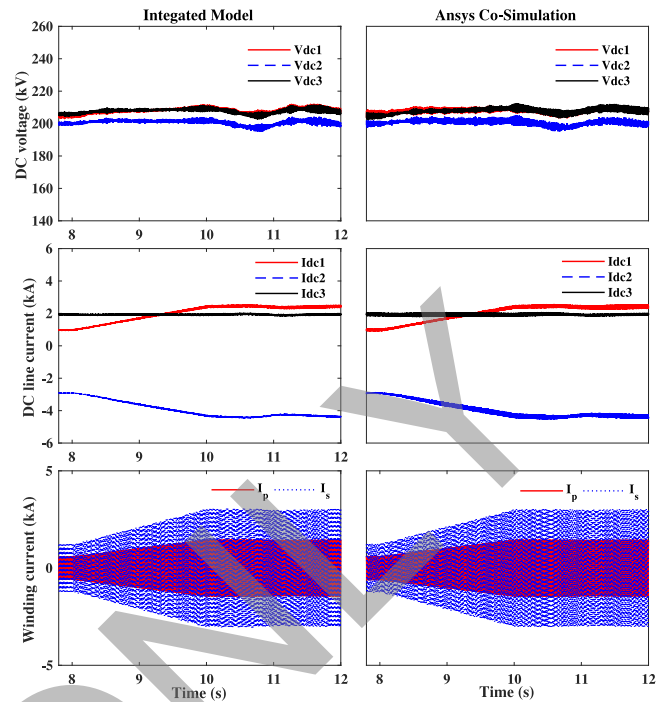


Fig. 10. MTdc system performance under power reversal.

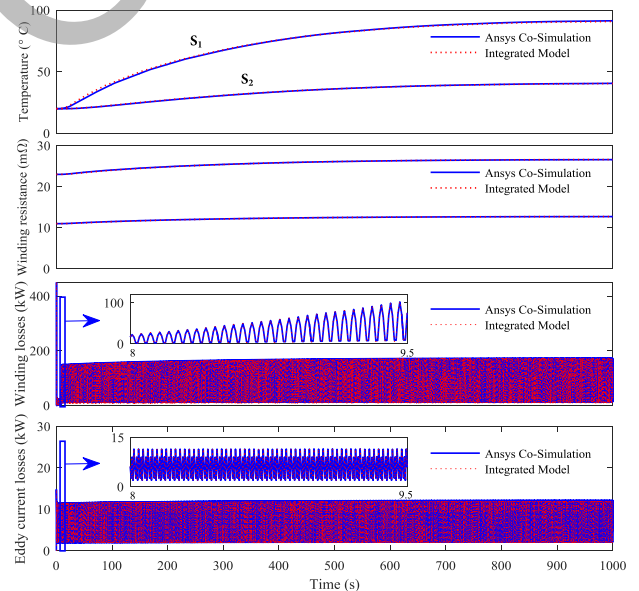


Fig. 11. Time-varying temperature, winding resistances, winding losses, and eddy-current losses of the FE transformer model.

the dc current at Station 1 rises from 1 to around 2.5 kA, and the power at the inverter station increases correspondingly as a combination of its counterparts. At the ac side of the rectifier conducting power reversal, the transformer currents on both the sides ramp up because of the increase in the power order. Ansys co-simulation, which shows the same results on the right column, demonstrates the accuracy of the proposed integrated model.

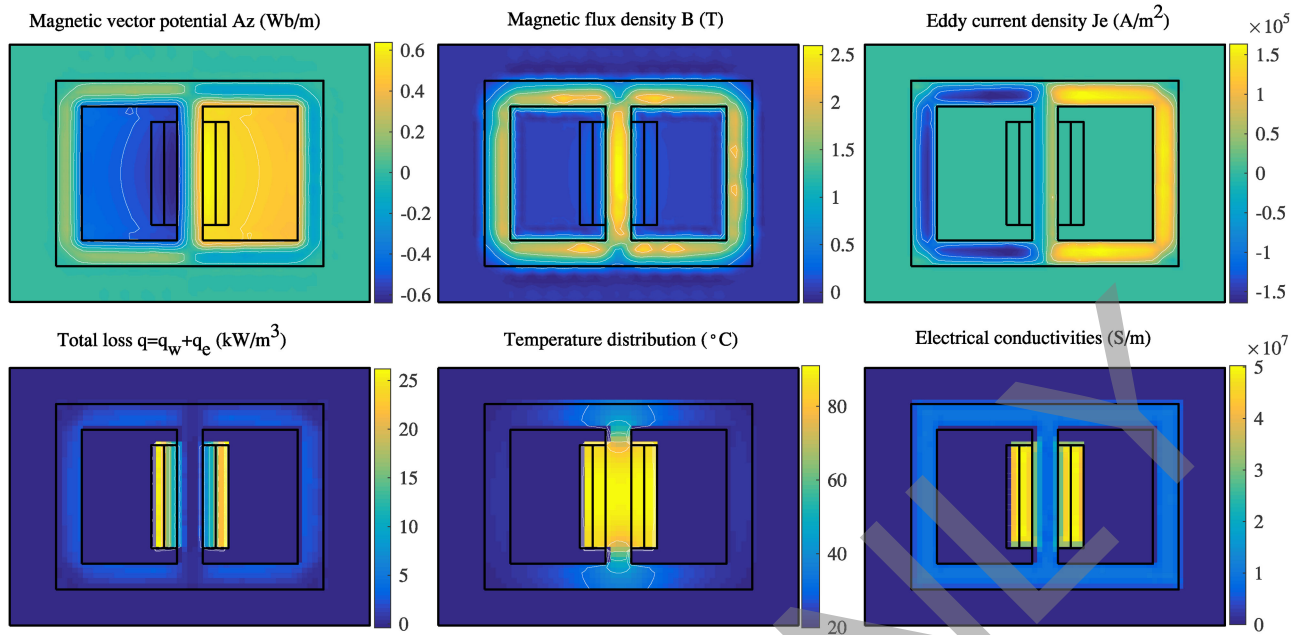


Fig. 12. Field distributions within the FE transformer ( $T_{r-1}$  phase A) at  $t = 1000$  s.

### C. FE Simulation Results

As mentioned before, the dense computation of FE models can contribute to a more comprehensive view of the physical details within the transformer. With the integrated thermo-electromagnetic model, all the transient fields can be available at any time point after post-processing. For example, at  $t = 1000$  s in the power reversal case study, the field distributions of the magnetic vector potential, magnetic-flux density, eddy-current density, winding loss and eddy-current loss, temperature, and the conductivities altered by temperature, are all plotted in Fig. 12.

Undoubtedly, these transient fields in practical working conditions can be very beneficial for designers to make better decisions on transformer problems such as loss reduction, saturation, and over-heating. In addition, the transient information related to such fields can also be monitored. Fig. 11 shows the time-varying temperature of sample locations  $S_1$  and  $S_2$  noted in the transformer core, how the winding resistance changes because of the thermal effects, the time-varying winding losses, and the total eddy-current losses. The steady-state thermal field is achieved after 20 min with the highest temperature of  $95^\circ\text{C}$  in the transformer core, and the total losses also increase until the material conductivities are altered by temperature anymore.

The Ansys co-simulation results are also plotted to evaluate the accuracy of the integrated model, and it turned out that the maximum error is less than 5%. Note that this error is mainly caused by the interfaces and the inherent assumptions between the thermal field, magnetic field, and external networks, because the FE-TLM block itself is quite accurate, and the error is less than 0.1%, compared with that using Ansys Maxwell when given the same input winding currents.

The massively parallelized codes executed on the NVIDIA Tesla V100 GPU with 5120 Cuda cores have high computational efficiency. The Ansys co-simulation was carried out on a workstation with dual Intel Xeon E5-2698 v4 CPUs, 20 cores

TABLE I  
EXECUTION TIME AND SPEEDUPS OF INTEGRATED MODEL PARALLELIZED ON GPU ( $10^5$  TIME-STEPS)

Cases	Number of FE Nodes	Ansys <sup>®</sup> co-sim Runtime	Integrated Model Runtime			Speedup
			FEM	MMC (5-513L)	Total	
Case 1	505	40.8h	0.72h	0.11-0.14h	0.86h	47.4
Case 2	1973	152.2h	2.53h	0.11-0.14h	2.67h	57.0
Case 3	4923	438.9h	7.94h	0.11-0.14h	8.08h	54.3

each, 2.2 GHz clock frequency, and 128 GB RAM. The Ansys HPC (high-performance computing) license was utilized and the available number of cores set to 40.

Table I shows the run-time comparison of Ansys HPC co-simulation and the integrated model on the GPU for FE problems of different sizes, and the total simulation time is 2 s with a time-step of  $20\ \mu\text{s}$  for the system. Although a time-step of  $1\ \mu\text{s}$  is applied to the MMC SMs, the coupled voltage and current sources exchange information every  $20\ \mu\text{s}$ . It takes Ansys co-simulations several days or even weeks to run  $10^5$  time-steps, while only several hours for the integrated model on GPU, and the speed-up is more than 47 times. On the other hand, the time MMC needs to run a simulation duration of 2 s is much shorter than that of the transformer, only 0.11 and 0.14 h when the MMC voltage levels are 5 and 513, respectively. Therefore, the simulation speedup is largely determined by the transformer's FEM model, as the overall speedup is still around 50 in all the three cases. It is also noticed that introducing the field-circuit interface as in Fig. 3 ensures independence between the two domains regarding the execution time.

As massively parallelizing the program, which is executed on modern GPU accelerating card, results in a smaller computational time incremental, the integrated model cannot only

provide more comprehensive physical details within transformers but also substantially decrease the design and test cycle for engineers to run an integrated simulation of ac/dc grids.

## VI. CONCLUSION

This paper proposed an integrated thermo-electromagnetic model to simulate the FE transformer transient interaction with MMC in multi-terminal dc grids. The comprehensive physical details, including the transient-field distributions within the transformer and device-level information of the MMC, can aid engineers to make better decisions on practical transformers and MMC problems such as material  $B-H$  properties, loss reduction, saturation, and power converter design guide, especially under transient conditions. The thermal field, magnetic field, and the electrical networks are fully coupled, and the information exchanges were implemented by extracting the coupling coefficients. The field-circuit coupling scheme, the FE transmission-line modeling solution, and the fine-grained MMC model, all have perfect parallelism, and the codes were sufficiently parallelized and implemented on Tesla V100 GPU to improve the computational efficiency. Consequently, the execution time of the integrated model is more than 47 times faster than that of the Ansys co-simulation while maintaining good accuracy, and the substantially reduced execution time enables more efficient design and test.

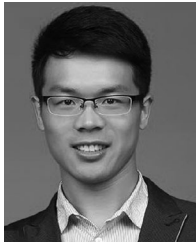
Future research will focus on the more accurate 3-D transformer FE modeling executed on GPUs to study the edge effects and faults, the hysteresis effect of the  $B-H$  curve, and the total losses will also consider the hysteresis influenced by the thermal field for integrated field-circuit simulation of the power system.

## APPENDIX

- 1) Material parameters: For copper,  $\alpha = 3.8 \times 10^{-11}$   $\Omega$  m/K and  $\sigma_0 = 5.8 \times 10^7$  S/m; for steel,  $\alpha = 5 \times 10^{-11}$   $\Omega$  m/K and  $\sigma_0 = 9.6 \times 10^6$  S/m.
- 2) MMC parameters: Voltage level 5–513, dc voltage  $V_{dc} = \pm 100$  kV, rated power 500 MW, ac voltage  $V_{ac} = 280$  kV; SM capacitor 3 mF, arm inductance 50 mH; dc line parameters: length 100 km,  $l = 0.05$  mH/km,  $r = 0.012$   $\Omega$ /km,  $c = 0.015$   $\mu$ F/km.
- 3) Transformer parameters: The size is 5.2 m  $\times$  3.6 m for the outer rectangle and 1.85 m  $\times$  2.6 m for the two inner rectangles. The coil size is 0.25 m  $\times$  2 m, and the number of coil turns is 418 for the primary side and 200 for the secondary side.

## REFERENCES

- [1] X. Song, V. Pickert, B. Ji, R. T. Naayagi, C. Wang, and Y. Yerasimou, "Questionnaire-based discussion of finite element multiphysics simulation software in power electronics," *IEEE Trans. Power Electron.*, vol. 33, no. 8, pp. 7010–7020, Aug. 2018.
- [2] Z. Yu *et al.*, "Simulation analysis on conducted EMD caused by valves in  $\pm 800$  kV UHVdc converter station," *IEEE Trans. Electromagn. Compat.*, vol. 51, no. 2, pp. 236–244, May 2009.
- [3] L. Liu, X. Cui, and L. Qi, "Simulation of electromagnetic transients of the bus bar in substation by the time-domain finite-element method," *IEEE Trans. Electromagn. Compat.*, vol. 51, no. 4, pp. 1017–1025, Nov. 2009.
- [4] S. Jahdi, O. Alatise, L. Ran, and P. Mawby, "Accurate analytical modeling for switching energy of PiN diodes reverse recovery," *IEEE Trans. Ind. Electron.*, vol. 62, no. 3, pp. 1461–1470, Mar. 2015.
- [5] Y. Huangfu, S. Wang, L. di Rienzo, and J. Zhu, "Radiated EMI modeling and performance analysis of a PWM PMSM drive system based on field-circuit coupled FEM," *IEEE Trans. Magn.*, vol. 53, no. 11, pp. 1–4, Nov. 2017.
- [6] E. Melgoza, R. Escarela-Perez, J. L. Guardado, and M. A. Arjona-Lpez, "Strong coupling of an electromagnetic transients program and a finite element magnetic field solver including eddy currents," *IEEE Trans. Power Del.*, vol. 32, no. 3, pp. 1414–1421, Jun. 2017.
- [7] W. Liang, J. Wang, T. Lu, and W. Fang, "A new method for multiple finite-element models in cosimulation with electrical circuit using machine multiloop modeling scheme," *IEEE Trans. Ind. Electron.*, vol. 61, no. 12, pp. 6583–6590, Dec. 2014.
- [8] J. Wu, J. Wang, C. Gan, Q. Sun, and W. Kong, "Efficiency optimization of PMSM drives using field-circuit coupled FEM for EV/HEV applications," *IEEE Access*, vol. 6, pp. 15 192–15 201, 2018.
- [9] B. S. Umesh and K. Sivakumar, "Pole-phase modulated multiphase induction motor drive with reduced torque ripple and improved dc link utilization," *IEEE Trans. Power Electron.*, vol. 32, no. 10, pp. 7862–7869, Oct. 2017.
- [10] F. Xu, V. Dinavahi, and X. Xu, "Parallel computation of wrench model for commutated magnetically levitated planar actuator," *IEEE Trans. Ind. Electron.*, vol. 63, no. 12, pp. 7621–7631, Dec. 2016.
- [11] J.-M. Jin, *The Finite Element Method in Electromagnetics*. Hoboken, NJ, USA: Wiley, 2015.
- [12] W. Wang *et al.*, "Massively parallel simulation of large-scale electromagnetic problems using one high-performance computing scheme and domain decomposition method," *IEEE Trans. Electromagn. Compat.*, vol. 59, no. 5, pp. 1523–1531, Oct. 2017.
- [13] P. Liu and V. Dinavahi, "Matrix-free nodal domain decomposition with relaxation for massively parallel finite-element computation of EM apparatus," *IEEE Trans. Magn.*, vol. 54, no. 9, pp. 1–7, Sep. 2018.
- [14] M. Unno, S. Aono, and H. Asai, "GPU-based massively parallel 3-D HIE-FDTD method for high-speed electromagnetic field simulation," *IEEE Trans. Electromagn. Compat.*, vol. 54, no. 4, pp. 912–921, Aug. 2012.
- [15] M. Namdari, M. Khosravi-Farsani, R. Moini, and S. H. H. Sadeghi, "An efficient parallel 3-D FDTD method for calculating lightning-induced disturbances on overhead lines in the presence of surge arresters," *IEEE Trans. Electromagn. Compat.*, vol. 57, no. 6, pp. 1593–1600, Dec. 2015.
- [16] Z. Zhou and V. Dinavahi, "Fine-grained network decomposition for massively parallel electromagnetic transient simulation of large power systems," *IEEE Power Energy Technol. Syst. J.*, vol. 4, no. 3, pp. 51–64, Sep. 2017.
- [17] N. Lin and V. Dinavahi, "Exact nonlinear micro-modeling for fine-grained parallel EMT simulation of MTdc grid interaction with wind farm," *IEEE Trans. Ind. Electron.*, vol. 66, no. 8, pp. 6427–6436, Aug. 2019.
- [18] G. M. Amdahl, "Computer architecture and Amdahl's law," *Computer*, vol. 46, no. 12, pp. 38–46, Dec. 2013.
- [19] O. Deblecker, J. Lobry, and C. Broche, "Novel algorithm based on transmission-line modeling in the finite-element method for nonlinear quasi-static field analysis," *IEEE Trans. Magn.*, vol. 39, no. 1, pp. 529–538, Jan. 2003.
- [20] P. Liu and V. Dinavahi, "Real-time finite-element simulation of electromagnetic transients of transformer on FPGA," *IEEE Trans. Power Del.*, vol. 33, no. 4, pp. 1991–2001, Aug. 2018.
- [21] 2019. [Online]. Available: <https://images.nvidia.com/content/technologies/volta/pdf/tesla-volta-v100-datasheet-letter-fnl-web.pdf>
- [22] Free BH Curves – Magweb, 2019. [Online]. Available: <http://magweb.us/free-bh-curves/>
- [23] K. Preis, O. Biro, G. Buchgraber, and I. Ticar, "Thermal-electromagnetic coupling in the finite-element simulation of power transformers," *IEEE Trans. Magn.*, vol. 42, no. 4, pp. 999–1002, Apr. 2006.
- [24] N. Lin and V. Dinavahi, "Dynamic electro-magnetic-thermal modeling of MMC-based dc/dc converter for real-time simulation of MTdc grid," *IEEE Trans. Power Del.*, vol. 33, no. 3, pp. 1337–1347, Jun. 2018.
- [25] R. Wachal *et al.*, "Guide for the development of models for HVdc converters in a HVdc grid," *Cigré TB604 (WG B4. 57)*, Paris, France, Tech. Rep., 2014.
- [26] 5SNA 2000K450300 StakPak IGBT Module, 2018. [Online]. Available: <https://new.abb.com/semiconductors/stakpak>
- [27] M. Hagiwara and H. Akagi, "Control and experiment of pulswidth-modulated modular multilevel converters," *IEEE Trans. Power Electron.*, vol. 24, no. 7, pp. 1737–1746, Jul. 2009.



**Peng Liu** (S'15) received the B.Sc. and M.Eng. degrees in electrical engineering from the Harbin Institute of Technology, Harbin, China, in 2013 and 2015, respectively. Currently, he is working toward the Ph.D. degree at the Department of Electrical and Computer Engineering, University of Alberta, Edmonton, AB, Canada.

His research interests include computational electromagnetics, finite element analysis, and parallel and distributed processing.



**Venkata Dinavahi** (S'94–M'00–SM'08) received the B.Eng. degree in electrical engineering from the Visveswaraya National Institute of Technology (VNIT), Nagpur, India, in 1993, the M.Tech. degree in electrical engineering from the Indian Institute of Technology (IIT) Kanpur, Kanpur, India, in 1996, and the Ph.D. degree in electrical and computer engineering from the University of Toronto, Toronto, ON, Canada, in 2000.

Presently he is a Professor with the Department of Electrical and Computer engineering, University of Alberta, Edmonton, AB, Canada. His research interests include real-time simulation of power systems and power electronic systems, electromagnetic transients, device-level modeling, large-scale systems, and parallel and distributed computing.



**Ning Lin** (S'17) received the B.Sc. and M.Sc. degrees in electrical engineering from Zhejiang University, Hangzhou, China, in 2008 and 2011, respectively, and the Ph.D. degree in electrical and computer engineering from the University of Alberta, Edmonton, AB, Canada, in 2018.

From 2011 to 2014, he was an Engineer on the flexible ac transmission system and high-voltage direct current power transmission. Currently, he is an Assistant Researcher with the University of Alberta.

His research interests include real-time simulation of power systems, power electronics, and high-performance computing.

READ ONLY